Module 3: Velocity Measurement

Lecture 16: Validation of PIV with HWA

The Lecture Contains:

- Hotwire Anemometry
  - Hotwire Measurements
  - Calibration Methodology
  - Curve Fitting
  - Directional Probe Senstivity
  - Data Reduction
- Uncertainity
- Validation of Experiments
  - Comparision of Hot Wire and PIV data
  - Drag Coefficient
  - Strouhal Number
  - Secondary Vorticity Pattern

Previous Next

Hotwire Anemometry

High temporal resolution is possible with a hotwire anemometer, though the attendant disadvantages of intrusive effects and low spatial resolution are equally significant. The principle of operation of a hotwire anemometer is briefly described below.

The output of a hotwire anemometer depends on convective heat transfer from a very fine (micron-sized) heated wire to the flowing fluid. The thermal equilibrium of the wire placed in a fluid medium gives the following energy balance relationship

$$H_{convec} + \dot{E} = i^2 R_{\omega} \tag{2}$$

Here $\mathrm{H_{convec}} = \mathrm{hA\,(T_w - T_f)}$ and $\dot{E}$ is the change in internal energy of the wire. Further, A is the surface area of hotwire per unit length in units of m, h is the convective heat transfer coefficient, $\mathrm{W\,^\circ C^{-1}}\ m^{-2}, T_w$ is the temprature of wire, $^\circ\mathrm{C}, T_f$ is the temperature of fluid, $^\circ C, i$ is the current flowing through wire, Amp, and R_w is the resistance of wire Ω. One can write

$$\dot{\mathrm{E}} = \mathrm{mC}\,\frac{\mathrm{dT_w}}{\mathrm{dt}} \tag{3}$$

where m is the mass of wire per unit length, $\mathrm{kg/m}$ and C is the specific heat of the wire material $\mathrm{Jkg^{-1}{}^\circ C^{-1}}$. The differential equation governing time-dependent convective heat transfer is now expressed as

$$mC\frac{dT_w}{dt} + Ah\left(T_w - T_f\right) - i^2 R_w = 0 \tag{4}$$

The quantity of interest in the above formulation is the convective heat transfer coefficient *h*. The rate of change of internal energy is practically zero for the CTA (constant temperature anemometer) mode of the hotwire. This approximation leads to the equation

$$\mathrm{H_{convec}} = 2\pi \mathrm{K_f l\,(T_w - T_f)\,Nu} \tag{5}$$

where $Nu = \dfrac{hd}{K_f}$ is the Nusselt number, d is the sensor diameter, K_f is the thermal conductivity of fluid, and ℓ is the length of the sensitive area of the hotwire probe.

Previous Next

The term which contains the effects of fluid velocity, temperature of the wire and the fluid temperature is Nusselt number. The general expression for Nusselt number in forced convective heat transfer for incompressible flow is given by

$$\mathrm{Nu} = f\left(\mathrm{Re}, \mathrm{Pr}, \mathrm{a1}, \mathrm{Gr}, \mathrm{Ma}, \gamma, a_T, 2\frac{l}{d'}\frac{K_f}{K_w}\right) \qquad (6)$$

where $\mathrm{Re} = \frac{U_c d}{\nu}$ is the Reynolds number, U_c is the effective cooling velocity, ν is the kinematic viscosity of fluid, Pr is the fluid Prandtl number, C_p is the specific heat of the fluid at constant pressure, $a1$ is the angle between the free stream direction and the normal to wire, Gr is Grash off number, Ma is Mach number, $\gamma = \frac{C_p}{C_v'}$ C_v is the specific heat of fluid at constant volume, and $a_T = \frac{T_w - T_f}{T_f}$ is the temperature loading or overheat ratio. Further, k_w and k_f are the thermal conductivities of the wire material and the fluid medium respectively. Fortunately, most applications permit a significant reduction in the number of parameters that must be included. The reasons are:

1 Forced convection parallel to the wire is small.

2. Prandtl number depends only on fluid properties.

3. Buoyancy effects can be neglected for $\mathrm{Gr} \times \mathrm{Pr} < \mathrm{Re}^2$. This expression shows that for air velocities greater than about 5.2 cm/s, buoyancy effects can be neglected.

4. For near atmospheric conditions of pressure and temperature and low velocities, Mach number is negligibly small.

5. Over a suitable range of temperatures (where HWA is commonly employed) C_p *and* C_v can be assumed to be constant.

Previous Next

The general equation governing the operation of hotwire can be now be simplified to

$$\mathrm{Nu} = f(\mathrm{Re}, a_T) \tag{7}$$

In isothermal flow measurements Equation 7 can be further simplified as

$$\mathrm{Nu} = f(\mathrm{Re}) \tag{8}$$

A relationship between Nusselt number and Reynolds number with a_T as a parameter that can be reliably used for converting the voltage output of the anemometer into velocity cannot be analytically derived. The analytical solution of flow past a circular cylinder for a wire-diameter based Reynolds number less than 40 shows that a power law relation is generally valid. The value of the exponent is 0.5 when the wire is taken to be infinitely long, flow is two dimensional and fluid properties are independent of temperature. However, the exponent depends on the geometric and physical properties of the wire, physical properties of fluid, and interference effects due to the prongs. A value of 0.45 is generally preferred; other empirical correlations derived using individual calibration of the wires is recommended in hotwire applications. (Chew and Simpson, 1988)

Previous Next

Hotwire measurements

Velocity was measured using a two channel hot wire anemometer along with an × -wire probe. The × was formed in the vertical plane, with the cylinder placed in the horizontal position. The probe was mounted on a traversing mechanism that facilitates all three orthogonal movements, to a positional accuracy in the most significant direction, namely the vertical at $\pm 0.1 mm$. The commercially available $DANTEC$ anemometer and probes were employed in the present work. The two wires of the probe were calibrated in the wind tunnel itself. Small changes in room temperature $(\pm 1^{o} C)$ were compensated through the use of a correction formula that assumes a temperature-independent heat transfer coefficient over this range. The probe was recalibrated for larger changes in room temperature. Both wires were operated at $150^{o} C$, and their calibration curves were seen to be almost identical. The assumption of equal sensitivity coefficients of the two wires was occasionally employed during data reduction. The calibration curves were smoothed using a fifth order polynomial. A pitot-static tube connected to a 19:99 mm of H_2O (Furness Controls) digital manometer was used for calibration. Both DC and RMS values of voltages were recorded using true voltmeters supplied by the manufacturer. Integration time of typically 100 s was used to obtain all time-averaged quantities. For the range of velocities considered in the present work (namely, 1-5 m/s), incompressible flow conditions have been assumed to prevail for the sake of data analysis.

Before the start of measurements, the stability of the CTA bridge as well as the signal conditioner setup was checked. Static and dynamic balancing of the circuits had to be ensured. The static bridge balancing requires the use of a proper overheat setting while dynamic balancing is checked by square wave test.

Local time-averaged velocity and velocity fluctuations were measured using the ×-wire probe. The ×-wire probe was used for measuring two components of velocity along the x and y directions. The continuous output voltage from the anemometer was acquired independently for each wire via an analog to digital (A/D) converter. The filter settings were determined by examining the complete power spectrum of the velocity components. Voltage signals from the CTA were low-pass filtered at 1-3 kHz and highpass filtered at 0.1 Hz using the 56N20 amplifier/filter unit. Further, the 56N20 signal conditioner was used for amplifying the input signals with gain factors of 10. The anemometer output voltage was collected by a PC (HCL) through a data acquisition card (Keithley) with Lab VIEW software. In the low velocity regime, measurements with the pitot-static tube as well as the hotwire anemometer are prone to errors. These can arise from higher order physical phenomena as well as probe interference effects. The errors can be controlled by using a pitot-static tube of small diameter (3 mm in the present study); in addition the hotwire probe in the present work operated at a lower temperature (of around $150^{o} C$,). It was felt that the lower wire temperature minimized free convection and radiation errors, without excessive loss of sensitivity. The accuracy of measurement was validated by examining the published Strouhal number-Reynolds number data for a circular cylinder at low Reynolds numbers. The power spectra of the velocity fluctuations were determined using the FFT algorithm. The sampling frequency used was 1000 Hz, the signal length for RMS measurements being 20 seconds.

Previous Next

Calibration Methodology

There are different approaches available for hotwire calibration. Two important steps involved in any approach are data generation and curve fitting. Calibration data are generated by measuring the output of the anemometer when the probe is subjected to a flow with a known velocity and low turbulence levels. In principle, specially designed apparatus are used to generate high quality flow with uniform velocity, temperature and very low turbulence level $(\text{say} < 0.1\%)$. However, a test cell that has clean approach flow conditions can also be used to carry out an in situ calibration. In the present study, calibration has been performed in the test cell itself, very close to the inflow plane. A much wider range of expected velocity variation was covered during calibration. Air velocity was directly measured using a pitot-static tube with an external diameter of 3 mm, mounted along the centerline of the test section. Calibration data are generated by measuring the output of the anemometer when the probe is subjected to uniform known velocity.

Small changes in room temperature can occur over the day of the experiment. For changes up to $\pm 1^0 C$ the recorded data can be compensated through the use of a correction formula that assumes a constant heat transfer coefficient over this small temperature range . The anemometer output voltage is corrected as

$$E_{corr} = \sqrt{\left(\frac{T_w - T_0}{T_w - T_a}\right)} E_a \qquad (9)$$

Here E_a is the acquired voltage, T_w the sensor hot temperature, T_0 the ambient reference temperature at which calibration data is available, and T_a is the ambient temperature during the experiment. In the present work, the probe was re-calibrated for larger changes in room temperature.

Previous Next

Curve Fitting

A number of functions for curve fitting the hotwire calibration data have been proposed in the literature. These functions are individually applied to the two wires of the × probe. The most commonly used functions are polynomials, power laws (King's law) and look-up tables. Low order polynomials, say second or third, do not show an oscillatory trend between calibration points. Jorgensen (2002) has shown that for a wide range of velocities $(0.2 - 60\ \mathrm{m/s})$ power law fits are less accurate than polynomial ts and show a systematic error distribution. The fourth- and fifth-order polynomials are preferable and gives less error, almost of equal accuracy. The reported maximum errors for these polynomials are 0.74 and 0.53% respectively.

For velocity measurements in the lower range, say 0.5 to 4 m/s, a number of special calibration procedures is available. In present investigation, two different approaches were examined, but the difference between them was found to be negligible. These approaches are based on the linearizer function (recommended by DANTEC) and a high order polynomial. In linearizer approach the mathematical relationship used is

$$y = 10^{A+Bx+Ey} + Cx + D \qquad (10)$$

Here A,B,C,D and E are curve fitting parameters. They are selected to give a fluid velocity equal to 10 m/sec for a wire output of 10 V. The quantity y is the output quantity equal to normalized velocity of fluid, defined as

$$y = 10 \times \frac{U}{U_{max}} \qquad (11)$$

Previous Next

The velocity referred here is the effective fluid velocity (at normal incidence to the wire). Further, x is the normalized voltage defined as

$$x = 10 \times \left[\frac{E - E_0}{E_{max} - E_0}\right] \quad (12)$$

Where E_0 is the output of wire measured at zero velocity of fluid and E_{max} measured at maximum velocity of fluid U_{max}. The function given above can closely match the calibration data, but its nonlinearity is a source of computational complexity.

The parameters A,B,C,D and E are obtained by means of an iterative least square error approach as follows. For any calibration point Equation 10 will produce an error ϕ_i given by

$$\phi_i = y_i - \left[10^{A+Bx_i+Ey_i} + Cx_i + D\right]. \quad (13)$$

Previous Next

The least square approach requires the sum of errors at all calibration points to be minimum i.e.

$$\Phi = \sum_{i=1}^{n} \phi_i^2 = \sum_{i=1}^{n} \{y_i - [10^{A+Bx_i+Ey_i} + Cx_i + D]\}^2 \quad (14)$$

$$\text{and} \quad \frac{\partial \Phi}{\partial A} = \frac{\partial \Phi}{\partial B} = \frac{\partial \Phi}{\partial C} = \frac{\partial \Phi}{\partial D} = \frac{\partial \Phi}{\partial E} = 0. \quad (15)$$

Let I be any of the parameters A,B,C,D or E; then, the derivatives can be evaluated as

$$\frac{\partial \Phi}{\partial I} = 2 \sum_{i=1}^{n} \phi_i \frac{\partial \phi_i}{\partial I} = 0 \quad (16)$$

Each derivative has to be expanded algebraically and solved for the corresponding parameter. At this stage, other parameters would take on assumed values. When one cycle of calculations is completed, the procedure is repeated for the next iteration.

In the polynomial curve fitting approach the data points are fitted with fourth order polynomial functions. It has been found that the fourth- and fifth-order polynomials were of nearly equal accuracy (the maximum error being 0.27% for the velocity range 0.2-3.5 m/s of interest to the present work). With $C_0 - C_4$ as calibration parameters, the fourth order polynomial is of the form

$$U = C_0 + C_1E + C_2E^2 + C_3E^3 + C_4E^4 \quad (17)$$

Here, U is velocity and E is voltage. Typical calibration data and the 4^{th} order t are shown in Figure 3.33. It is also shown that the calibration curves for both wires operating at practically equal overheat ratios are very close to each other.

Previous Next

Directional probe sensitivity

Directional calibration of multi-sensor probes (×- or tri -axial) provides their individual directional sensitivity coefficients. These are yaw factor k_n and pitch-factor P_h. They are required to decompose effective velocities derived from the calibration data into velocity components in laboratory coordinates. The effective cooling velocity acting on a hot wire can be expressed by means of the normal (U_n), tangential (U_t) and binormal components (U_{bn}) modified by the yaw and pitch factors, k_n and P_h as follows:

$$U_{eff}^2 = U_n^2 + k_n^2 U_t^2 + P_h^2 U_{bn}^2 \qquad (18)$$

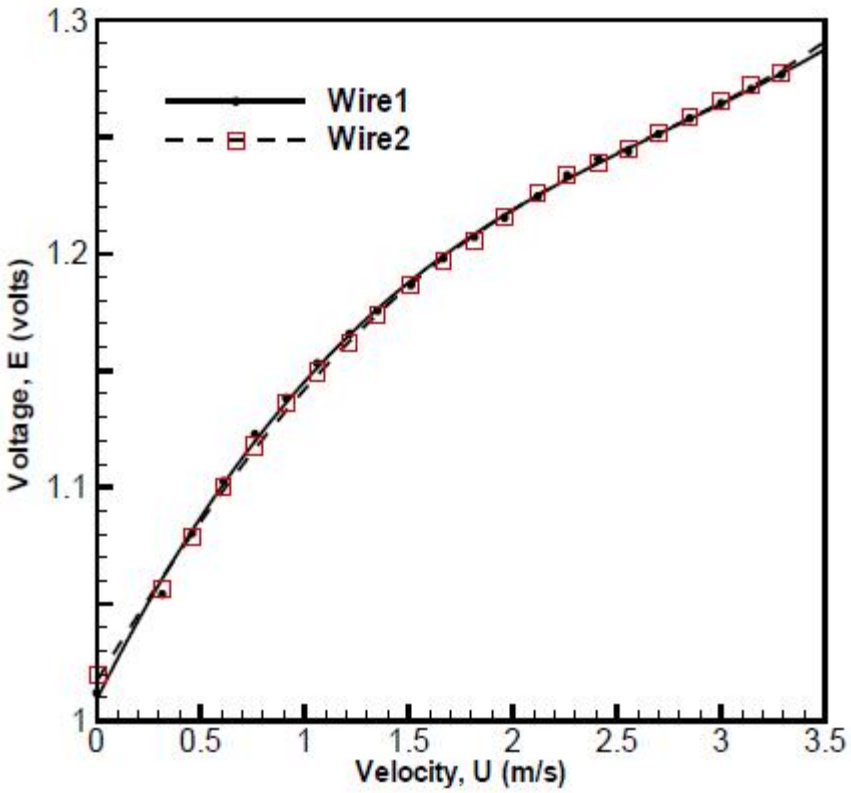

Figure 3.34: Calibration data for a ×-wire hotwire probe (symbols) compared with a fourth order curve tting formula (lines).

During directional calibration, the probe is turned through a number of inclination angles with respect to a known flow vector. In each position, U_n, U_t and U_{bn} are calculated from the probe velocity transfer function. This provides a set of equations for determining k_n and P_h for each wire in each angular position. The × - array probes uses the yaw coefficients, k_1 and k_2 in order to decompose the calibration velocities U_{cal1} and U_{cal2} into the U and V components. As the yaw coefficients, k_1 and k_2 depend only on the geometry, the directional calibration test is needed to be carried out only once in the life of the probe. In the present work, the freshly supplied probe (DANTEC probe 55P63) was used. The default values of k_1 and k_2 $(= 0.2)$ was used during analysis.

Data Reduction

The time-mean component of the voltage signal has been obtained independently through a $4\frac{1}{2}-\text{digit}$ voltmeter, DANTEC 56N22. In order to achieve the best utilization of the analog to digital converter resolution, the fluctuating component of the voltage signal has been amplified by a gain factor of 10, prior to acquisition in the PC. This approach has the advantage that integration time constants can be applied unrestrictedly on the time-mean and fluctuating component of the signal. A typical value of 100 s integration constant has been used to measure the time-mean voltage. The fluctuation part was acquired for 20 seconds duration with a gain setting of 10. The time-mean and the fluctuating voltage have been added during data processing to get the complete instantaneous signal. It has been subsequently used with the calibration equation to calculate the instantaneous velocity.

For the $\times$ -probes that are oriented at $\alpha = 45^{o}$ to the incoming flow direction and yaw coefficients $k_1^2 \; and \; k_2^2$ for each wire, the velocities $U_1(t) and \; U_2(t)$ in the wire coordinate system are related to the calibration velocity of each wire as

$$k_1^2 U_1^2 + U_2^2 = \frac{1}{2}(1 + k_1^2){U_{cal1}}^2 \tag{19}$$

$$U_1^2 + k_2^2 U_2^2 = \frac{1}{2}(1 + k_2^2){U_{ca2}}^2 \tag{20}$$

The above equations can be rearranged as:

$$U_1 = \frac{1}{\sqrt{2}}\sqrt{(1 + k_2^2){U_{cal2}}^2 - k_2^2 {U_{cal1}}^2} \tag{21}$$

$$U_2 = \frac{1}{\sqrt{2}}\sqrt{(1 + k_1^2){U_{cal1}}^2 - k_1^2 {U_{cal2}}^2} \tag{22}$$

Previous Next

The velocity components $U(t)$ and $V(t)$ in the laboratory coordinates x and y can be calculated from the velocity in the wire coordinate using an appropriate geometrical transformation, leading to:

$$U = \frac{1}{\sqrt{2}}U_1 + \frac{1}{\sqrt{2}}U_2 \quad (23)$$

$$V = \frac{1}{\sqrt{2}}U_1 - \frac{1}{\sqrt{2}}U_2 \quad (24)$$

The digitization of the hotwire signal results in N evenly distributed and statistically independent samples that, to a first approximation, can be taken as statistically stationary. The mean value of the velocities U and V can be evaluated as the ensemble average of the velocity signals $u(t)$ and $v(t)$, i.e.

$$U = \frac{1}{N}\sum_{i=1}^{N} u \quad (25)$$

$$V = \frac{1}{N}\sum_{i=1}^{N} v \quad (26)$$

Subsequently, the velocity fluctuations, $u'(t)$ and $v'(t)$ are calculated by subtracting the mean component of velocity from the velocity signals $U(t)$ and $V(t)$. Hence

$$u'(t) = u(t) - U \quad (27)$$

$$v'(t) = v(t) - V \quad (28)$$

The root mean square components of velocities, $\overline{u'^2}$, $\overline{v'^2}$ and the Reynolds shear stress $\overline{u'v'}$ have been evaluated as:

$$u_{rms} = \left[\frac{1}{N-1}\sum_{i=1}^{N}(u')^2\right]^{1/2} \quad (29)$$

$$v_{rms} = \left[\frac{1}{N-1}\sum_{i=1}^{N}(v')^2\right]^{1/2} \quad (30)$$

$$\overline{u'v'} = \frac{1}{N}\sum_{i=1}^{N} u'v' \quad (31)$$

Here, the measurements from the two wires of the probe are taken to be simultaneous. This assumption neglects the small time lag introduced during data transfer in the A/D card.

Previous Next

Uncertainty

The seeding of flow with oil particles, calibration, laser light reflection, background illumination, image digitization, cross correlation calculation, velocity gradients and out of- plane particle motion affect the accuracy of PIV measurements. Tracer particles need to follow the main air flow without any lag. For the particle size utilized and the range of frequencies in the wake, an expected slip velocity error of 0.3% to 0.5% relative to the instantaneous local velocity is expected. A second source of error in velocity measurement is due to the weight of the particle. In the present experiments, the effect of the weight of the seed particles was examined by conducting experiments at a fixed Reynolds number by varying the size of the cylinder and fixed in flow velocity. The streamline plot and the dimensionless size of the recirculation region were found to be identical in each case, and independent of the fluid velocity. The noise due to background light was minimized by using a band-pass filter (at the wavelength of the laser) before the camera sensor. The hotwire measurements are affected by the error due to calibration, free convection effect at small velocity, curve fitting error, electrical noise, digitization error and turbulence intensity in the incoming fluid stream. The pitot static tube, hotwire anemometry and PIV measurements of mean velocity compared exceedingly well with each other indicating less than 2% error in velocity measurements. The drag coefficient calculation has been carried out at various stream-wise location and found to be within 5% of each other. From repeated measurements at the zero degree cylinder orientation (Figure 3.35, with Reynolds number kept constant to within $\pm 1\%$), the uncertainty in drag coefficient has been determined to be within $\pm 5\%$. The Strouhal number has been calculated at different x and y locations from both u and v-velocity measurements indicating the uncertainty on Strouhal number to be $\pm 2\%$. The influence of particle density on the measured flow field is shown in Figure 3.36; the influence is seen to be small.

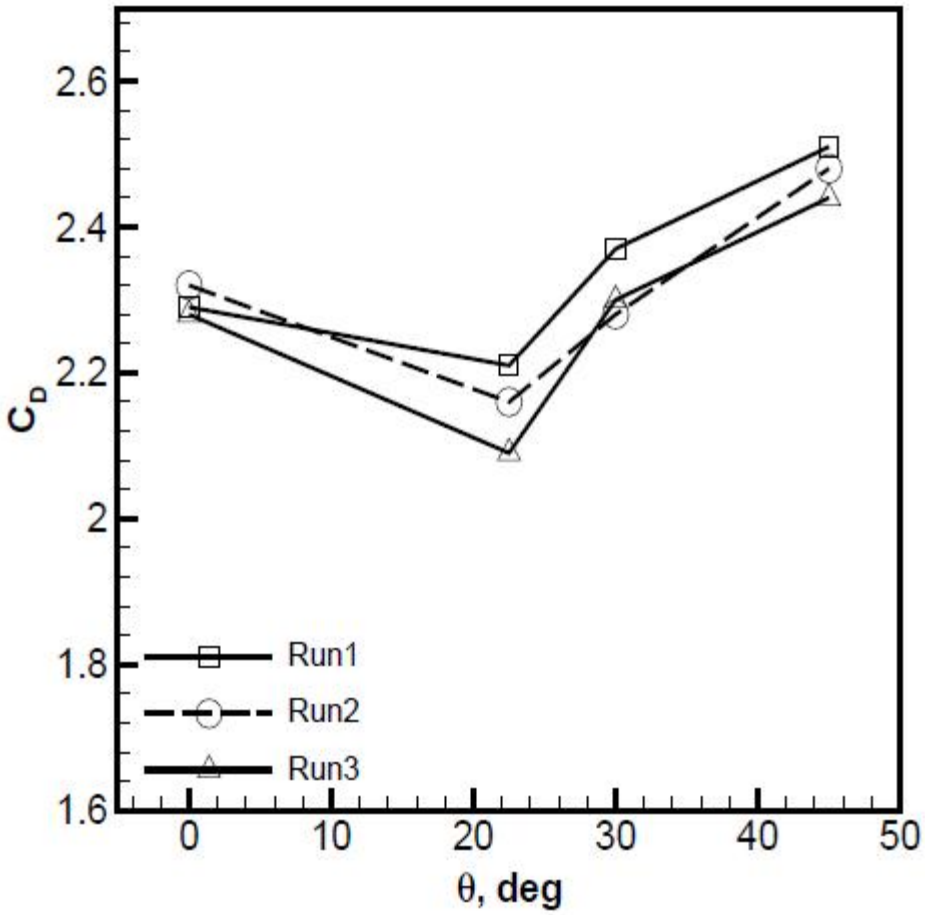

Figure 3.35: Variation of drag coefficient with cylinder orientation. Experiments were conducted on three different days under nominally similar conditions.

Previous Next

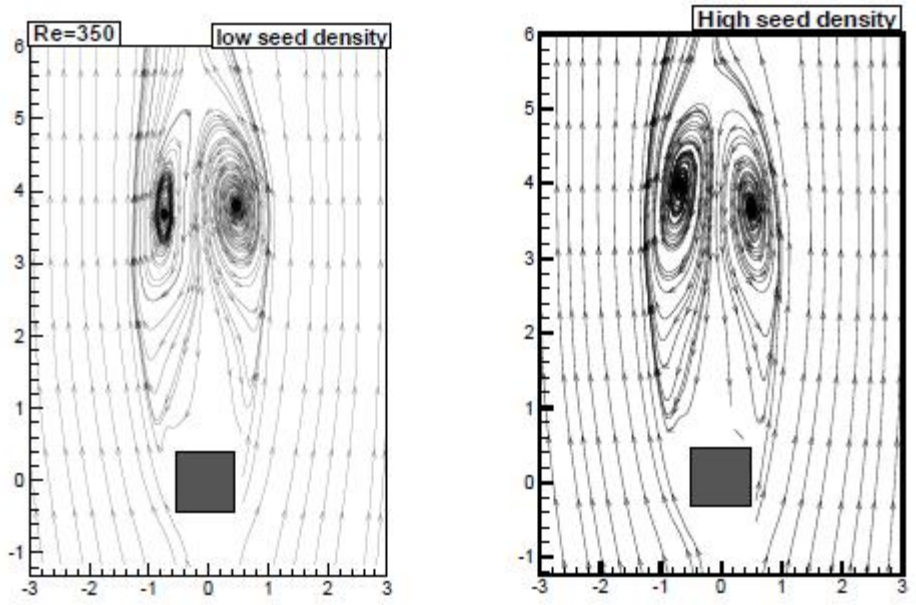

Figure 3.36: Effect of seeding density on the velocity field.

Previous Next

Validation Experiments

The validation of the experimental technique, data analysis procedure and computer implementation has been carried out in two ways: (i) Comparison between different measurement techniques, (ii) Comparison of the standard calculated quantities with that in the literature. The validation results of mean velocity, vorticity patterns, Strouhal number and drag coefficient are discussed in the following sections.

Comparison of hotwire and PIV data

Benchmark experiments were conducted at selected planes in the wake of the square cylinder under identical conditions. Both hotwire and PIV measurements were recorded. A cross-check in terms of the two components of time-averaged velocity is presented in Figures 3.37 to 3.41 at two different Reynolds number (Re=410 and 610). At x=5 the u-velocity profiles recorded by the two techniques show significant difference in the velocity deficit, Figure 3.37. Since the recirculation zone extends upto x=6, the time-averaged velocity is negative at all earlier x-locations. The hotwire probe cannot resolve the negative stream-wise velocity component, while PIV does not suffer from this drawback. Hence, adjacent to the cylinder, the PIV data can be assumed to be more accurate. As one moves downstream, the match between the two measurements is better. At x=15 units, the stream-wise velocity profiles from hotwire and PIV measurements merge with each other (figure 3.39).

Figure 3.38 to 3.40 compare the transverse v-velocity for cylinder at different orientations and Re=410 and 610. The overall trends in the v-velocity are similar. At x=5 location, the maximum deviation of v-velocity between hotwire and PIV measurements is within the uncertainty of the velocity measurements. This is in contrast to the high deviation in the u-velocity measurements in Figure 3.37. The hotwire measurement error in the recirculation zone is higher for the u-velocity than the v-velocity. The v-velocity trend at x=10 and 15 are similar between hotwire and PIV measurements. The higher percentage deviation of the v-velocity at these locations compared to the earlier x-location can be be attributed to the lower absolute magnitude of the v-velocity. Figure 3.43 shows the comparison of u_{rms} velocity at two x locations. At x=5 the PIV data shows a slightly higher peak RMS value compared to hotwire measurements. At x=10, both PIV and hotwire results coincide.

Previous Next

Drag coefficient

Table 1 presents a comparison of time-averaged drag coefficient of a square cylinder for zero angle of incidence; experiments as well as numerical simulation are compared. For three dimensional numerical simulation, the drag coefficient is a value averaged over the entire span of the cylinder. The experimental value is that of the cylinder mid-plane, obtained by a wake survey method. The drag coefficient from all studies are in the range of 1.95 to 2.32 and are comparable to each other.

Figure 3.44 shows the comparison of drag coefficient (C_D) with cylinder orientation from present experiments and two dimensional numerical simulation of Sohankar et al. (1998). The drag coefficient is based on the cylinder dimension rather than the projected area. The match is not good when we compare the mid-plane value with that of Sohankar (1998), possibly because of the dimensionality of the numerical simulation. The match improves when the 3-plane averaged value is compared with the cylinder average of three dimensional simulation. The minimum in the drag coefficient at 22.5^o is to be seen in both the mid-plane value as well as the average data. Sohankar et al. (1999) conducted a 3D numerical simulation of flow past a square cylinder at a low aspect ratio and found substantial variation in drag coefficient along the span-wise direction.

Previous Next

Module 3: Velocity Measurement

Lecture 16: Validation of PIV with HWA

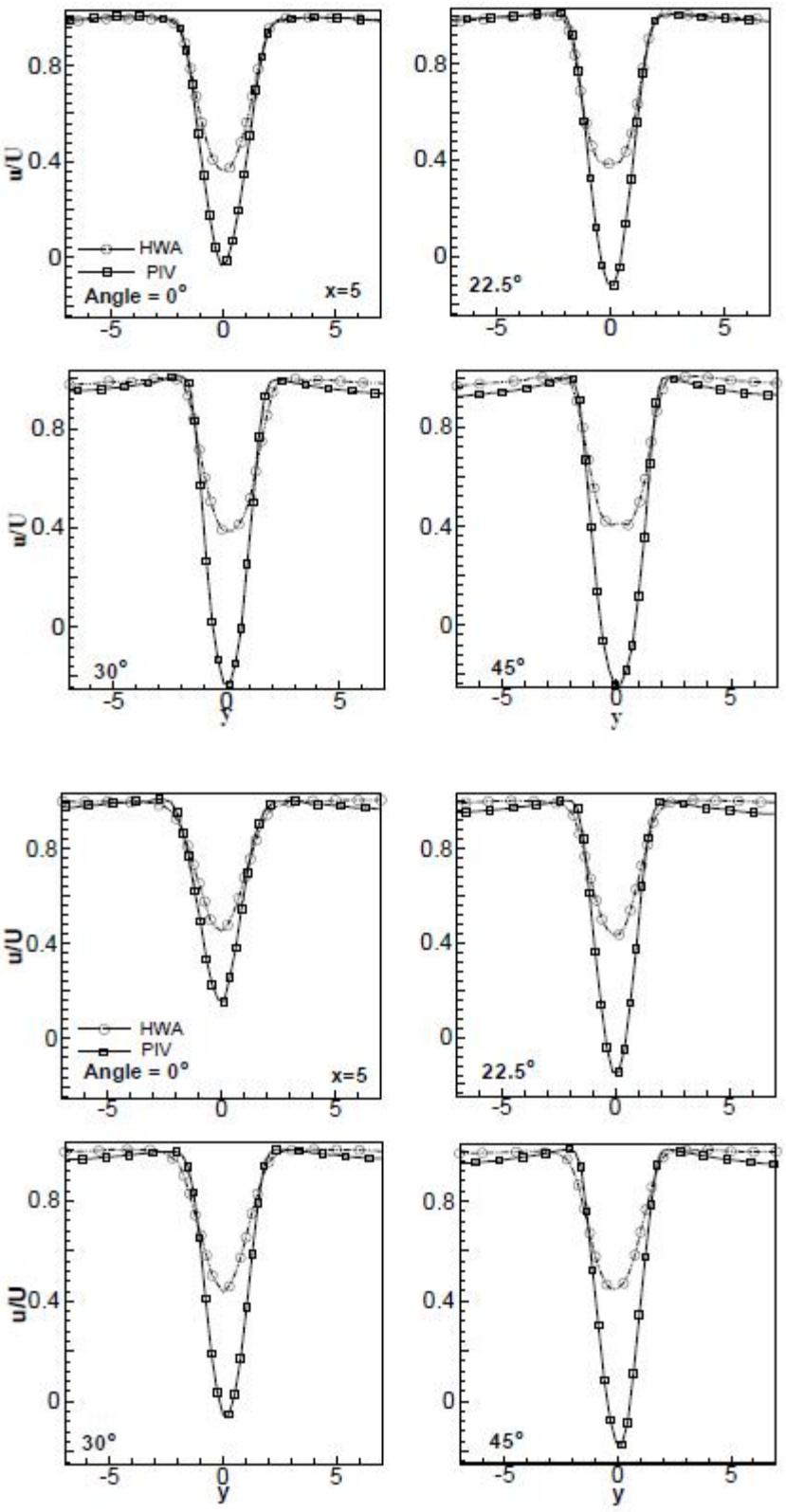

Figure 3.37: Comparison of time-averaged u-velocity profiles in the wake of a square cylinder. PIV and HWA measurements at four cylinder orientations (0, 22.5, 30 and 45^0) are presented at x = 5 location. Reynolds number=410(top) and 610(bottom).

Previous Next

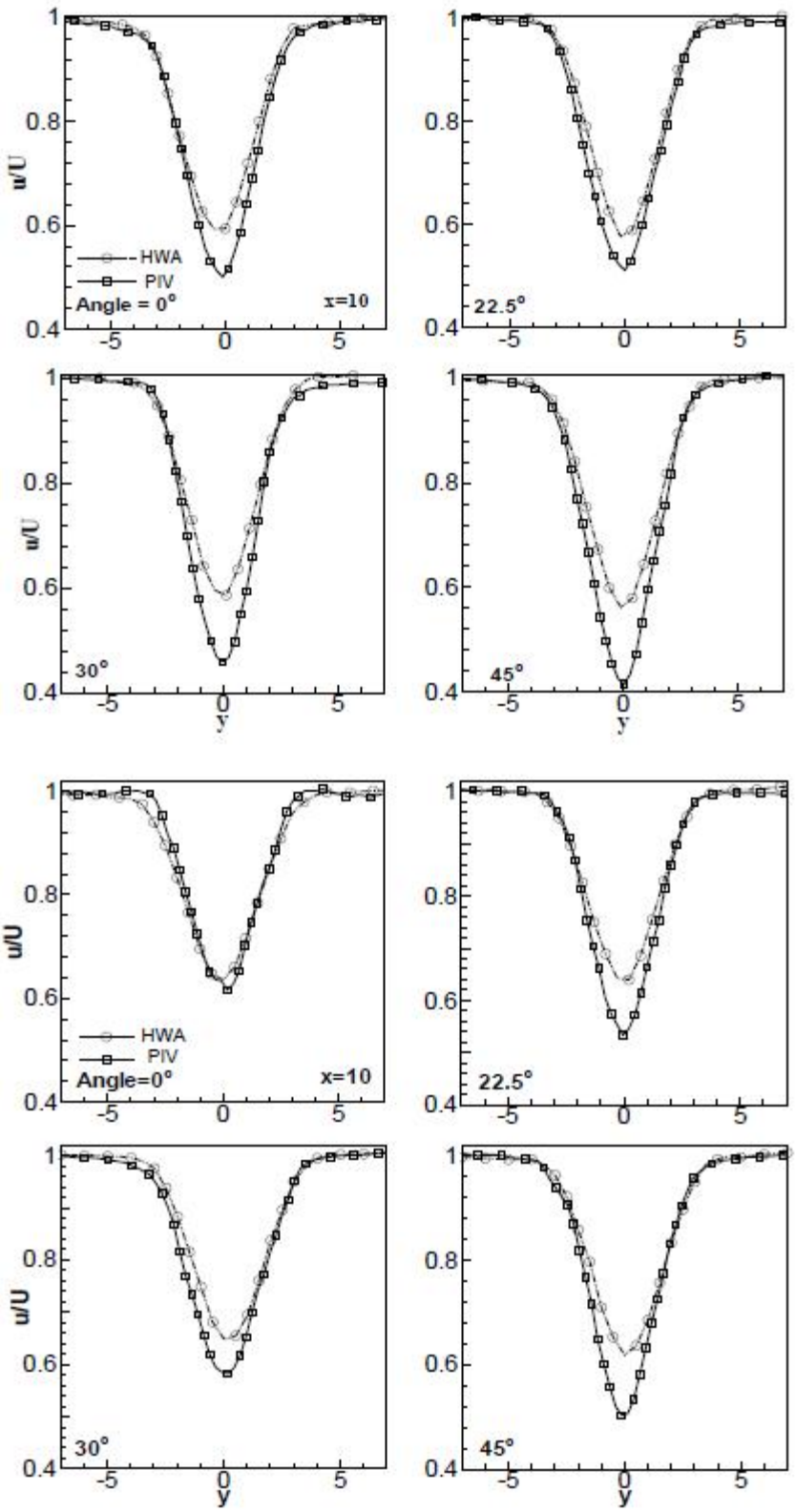

Fig 3.38: Comparison of time-averaged u-velocity proles in the wake of a square
cylinder. PIV and HWA measurements at four cylinder orientations (0, 22.5, 30 and

45^0) are presented at x = 10 location. Reynolds number=410(top) and 610(bottom).

Previous Next

Module 3: Velocity Measurement

Lecture 16: Validation of PIV with HWA

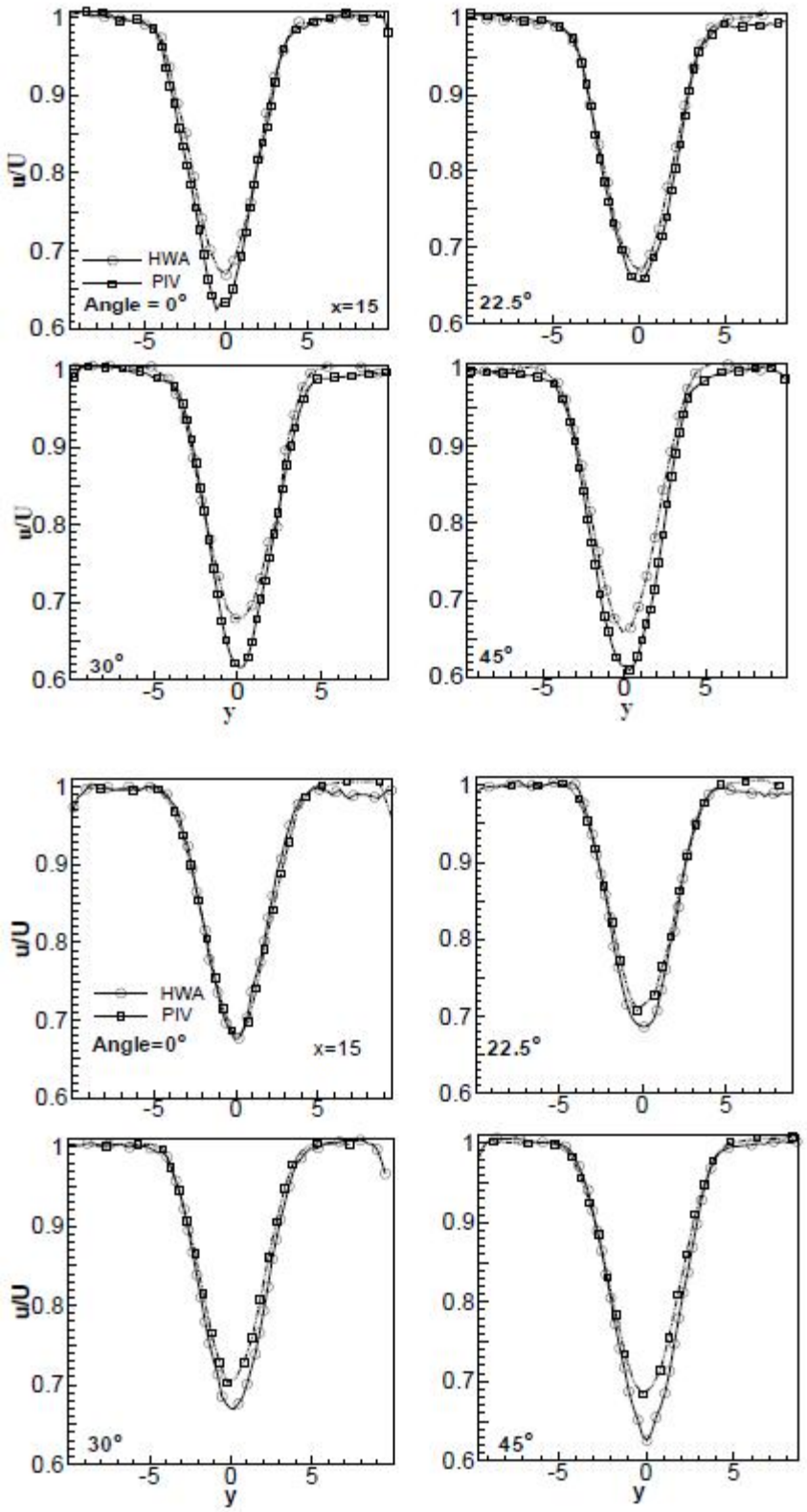

Figure 3.39: Comparison of time-averaged u-velocity proles in the wake of a square cylinder. PIV and HWA measurements at four cylinder orientations (0, 22.5, 30 and 45^0) are presented at x = 15 location. Reynolds number=410(top) and 610(bottom).

Previous Next

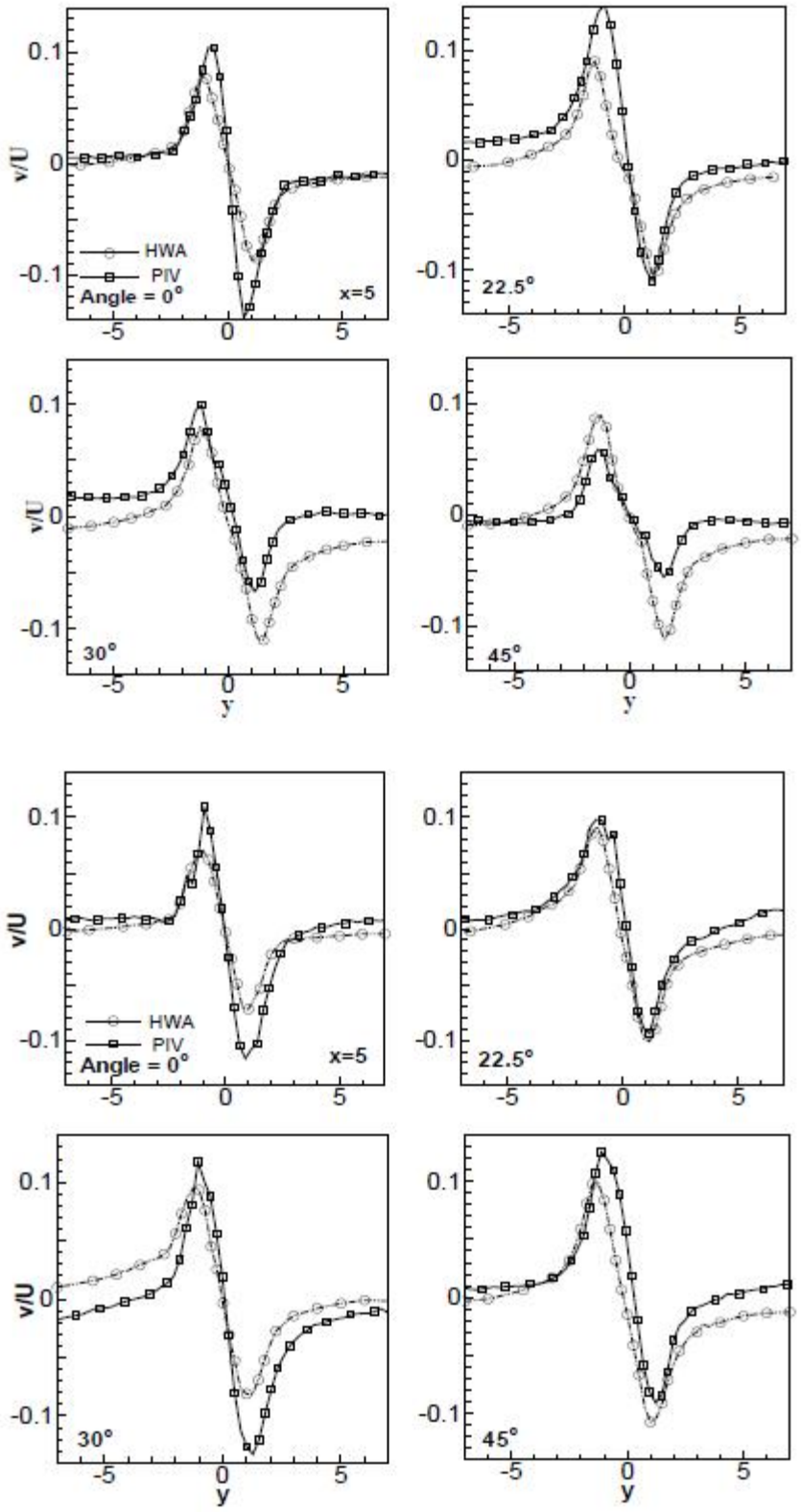

Figure 3.40: Comparison of time-averaged v-velocity proles in the wake of a square cylinder. PIV and HWA measurements at four cylinder orientations (0, 22.5, 30 and 45^0) are presented at x=5 location. Reynolds number=410(top) and 610(bottom).

Previous Next

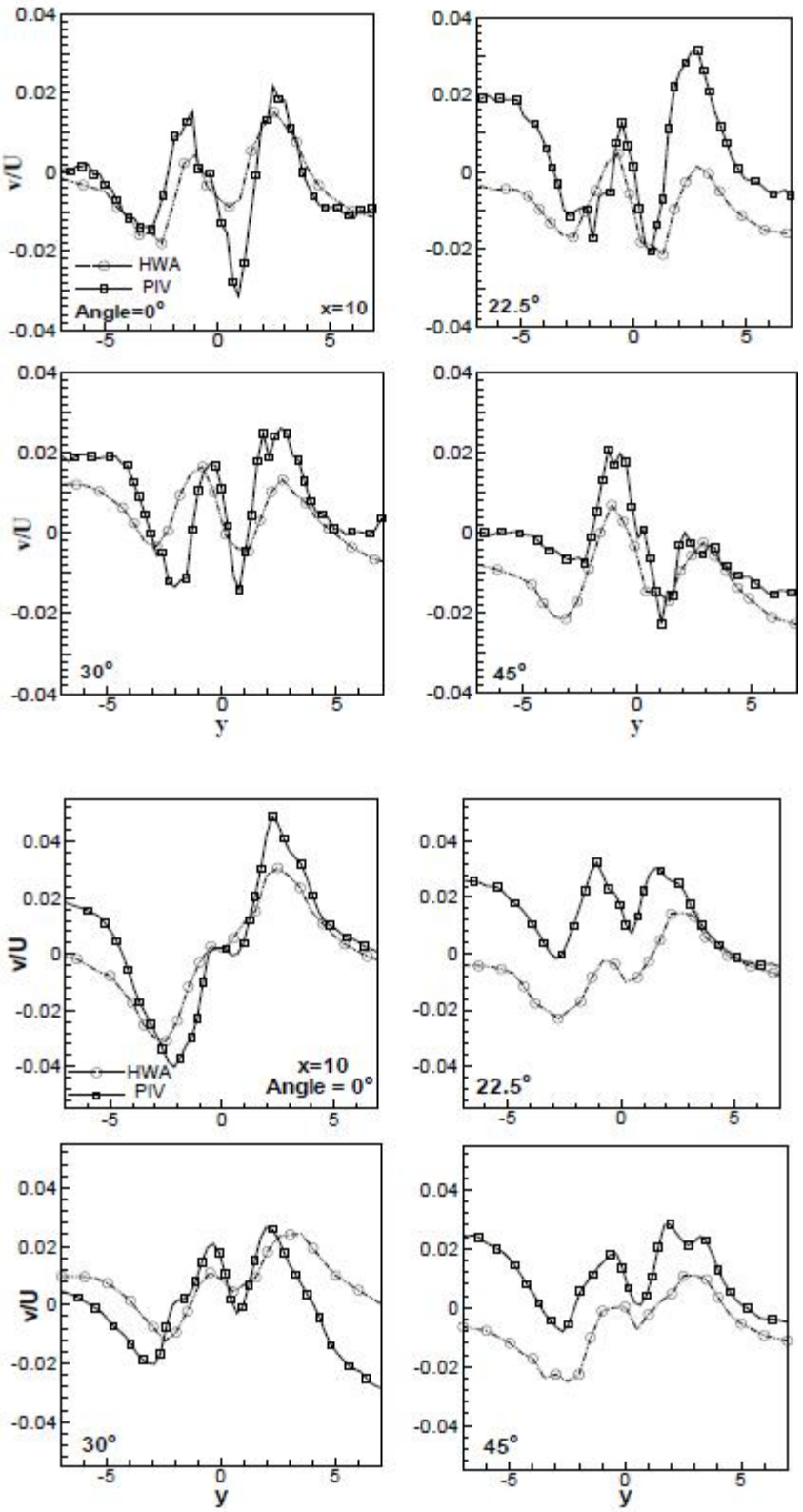

Figure 3.41: Comparison of time-averaged v-velocity proles in the wake of a square cylinder. PIV and HWA measurements at four cylinder orientations (0, 22.5, 30 and 45^0) are presented at x= 10 location. Reynolds number=410(top) and 610(bottom).

Previous Next

Module 3: Velocity Measurement

Lecture 16: Validation of PIV with HWA

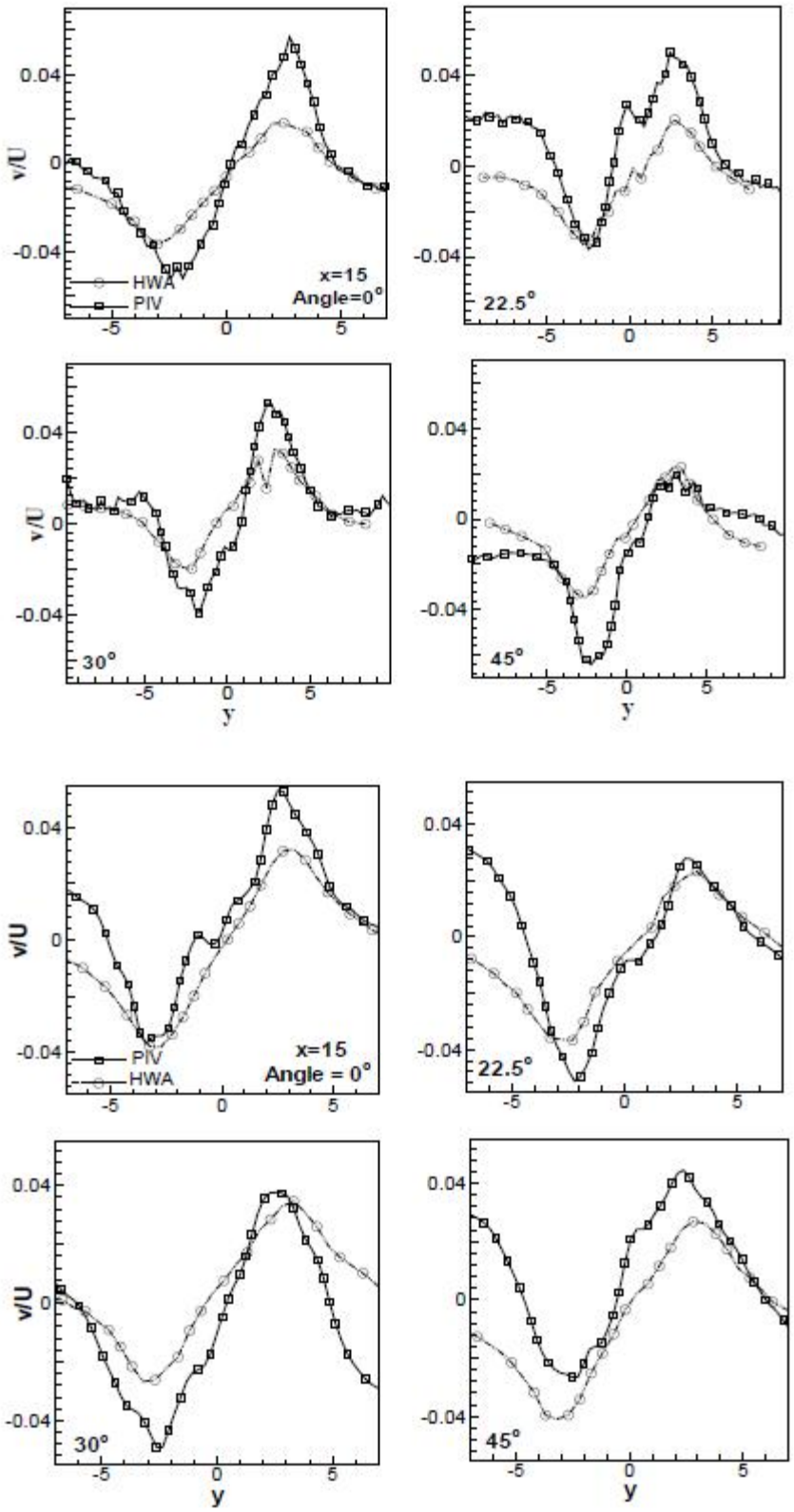

Figure 3.42: Comparison of time-averaged v-velocity proles in the wake of a square cylinder. PIV and HWA measurements at four cylinder orientations (0, 22.5, 30 and 45^0) are presented at x = 15 location. Reynolds number=410(top) and 610 (bottom).

Previous Next

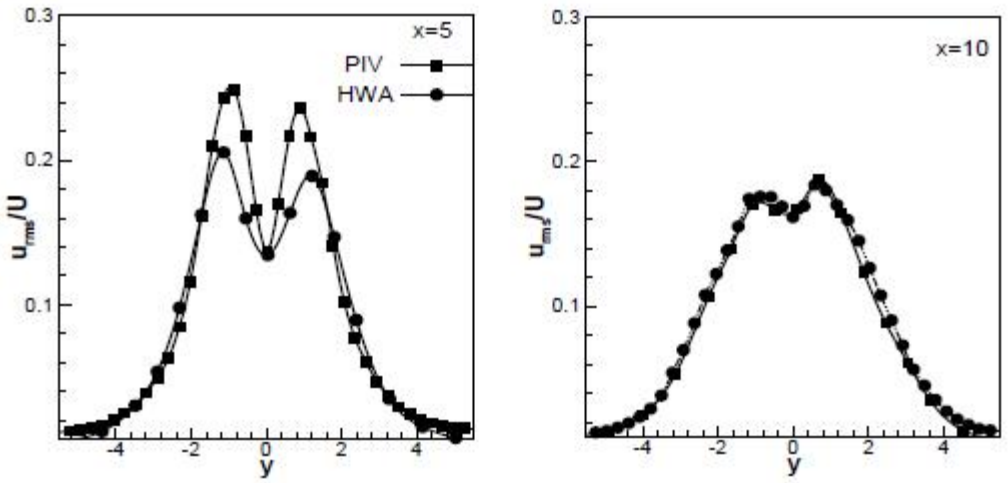

Figure 3.43: Comparison of u_{rms}velocity proles using PIV and HWA in the wake of a square cylinder at 0°cylinder orientation at two x locations (x=5 and 10).

Table 1: Comparison of drag coefficient with the published literature for flow past a square cylinder.

Authors	Nature of Study	Aspect ratio	Blockage	Re	$\bar{C}_D$
Davis et al. (1984)	Numerical (2D)	-	0.170	470	1.95
Sohankar et al. (1999)	Numerical (3D)	6	0.055	400	1.67
Saha et al. (2003)	Numerical (3D)	6-10	0.100	400	2.21
Present	Experimental	16	0.030	410	2.32
		28	0.060	420	2.03

Previous Next

Strouhal Number

Table 2 compares the Strouhal number from the present work with that of other investigations at similar Reynolds numbers and zero degree orientation. A maximum deviation of $\pm 7\%$ between the present work and that of other investigations is indicated in Table 2. The difference between the present study and literature can be attributed to the difference in aspect ratio, blockage and inlet turbulence level. Figure 3.45 shows the comparison of the present experiments with the published literature in terms of Strouhal number for a circular cylinder (top) and square cylinder (bottom). Various Reynolds numbers have been considered. Each individual data set shows only a weak dependence of Strouhal number on Reynolds number. A certain level of scatter is visible. Data recorded in the present experiments at aspect ratios 16, 28 and 60 are shown by shaded and unshaded diamonds and unshaded squares. Broadly, these three lines bound the Strouhal number values reported in the literature. Thus, one can conclude that aspect ratio can explain the minor discrepancy in Strouhal number data of a square cylinder. The experimental data of the present study in Figure 3.45 show that Strouhal number increases with an increase in aspect ratio. The trend recorded for a circular cylinder by Norberg (1994) is supported by the present study.

Table 2: Comparison of Strouhal number with the published literature for flow past a square cylinder.

Authors	Nature of Study	Aspect Ratio	Blockage	Re	St	Re	St
Okajima (1982)	Experimental	120	0.016	300	0.143	500	0.130
Davis et al. (1984)	Numerical (2D)	300	0.080	250	0.164	600	0.150
Sohankar et al. (1999)	Numerical (3D)	10	0.056	300	0.153	520	0.130
Saha et al. (2003)	Numerical (3D)	6-10	0.100	295	0.135	575	0.140
Present	Experimental	16	0.030	310	0.122	550	0.129
		28	0.060	310	0.153	516	0.140
		60	0.030	295	0.155	500	0.145

Previous Next

Secondary vorticity pattern

Figure 3.46 shows the instantaneous stream-wise vorticity contours (ω_x) above a circular cylinder obtained in the present work using PIV. The axis of the vorticity component is along the flow direction. The PIV results of Brede et al (1996) are shown for comparison. The Reynolds number of the present work is 330, while that of the reference is 290. At these Reynolds numbers, secondary (streamwise) vortices are generated along with the spanwise (Karman) vortices. The secondary vortices are arranged along a line parallel to the cylinder axis. The sense of rotation alternates along the spanwise direction. The secondary vortices correspond to mode B of Williamson (1997). The spanwise wavelength of the secondary vortices is around one cylinder diameter, the spacing between the vorticity peaks being, in general, a constant. These trends are realized in both sets of experiments. Overall, the favorable comparison of vorticity patterns with the published literature.

Note: The supplementary material accomparying Module 3 contains addtional PIV images for flow past a cylinder of square cross section.

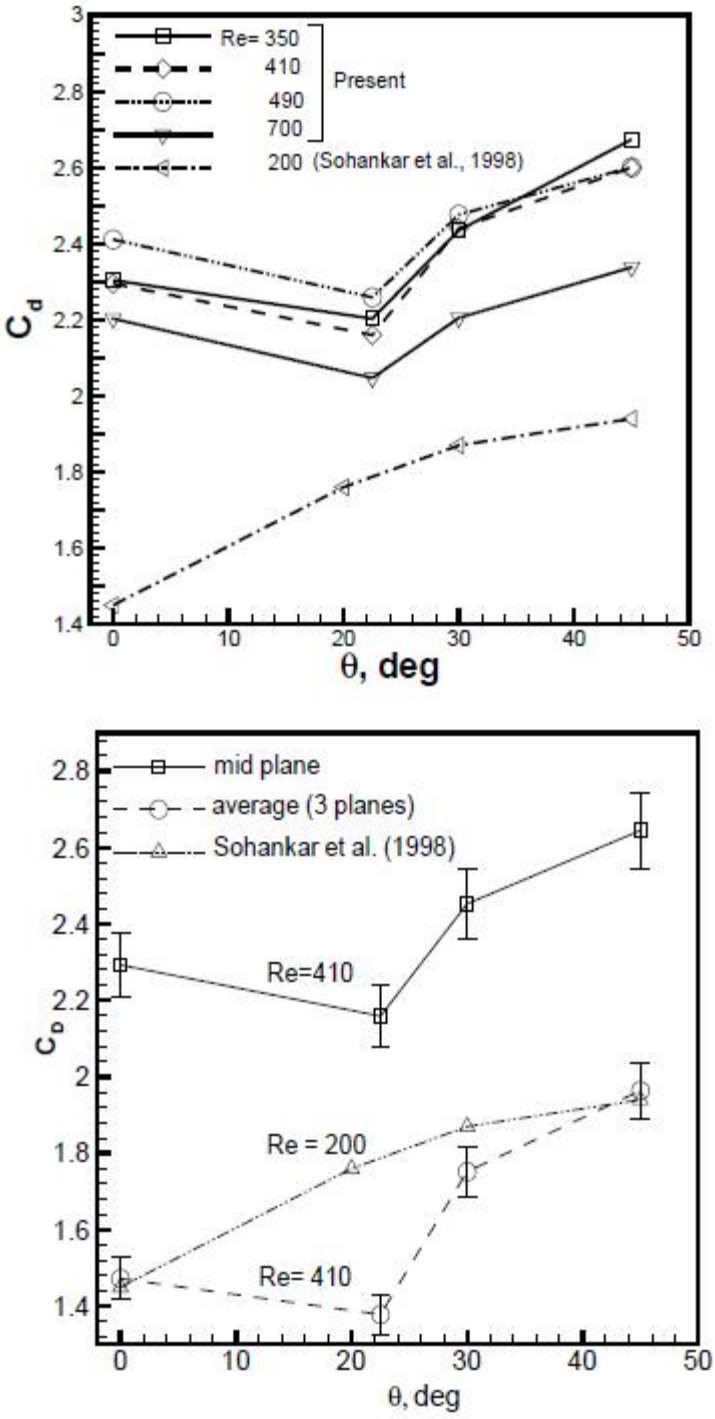

Figure 3.44: Variation of drag coefficient with incidence angle. The data of the present study in the top gure is for mid-plane of the cylinder. The numerical simulation of Sohankar et al. (1998) reports an average over the cylinder length. The drag coefficient data averaged over 3-planes has been shown in the bottom figure.

Previous Next

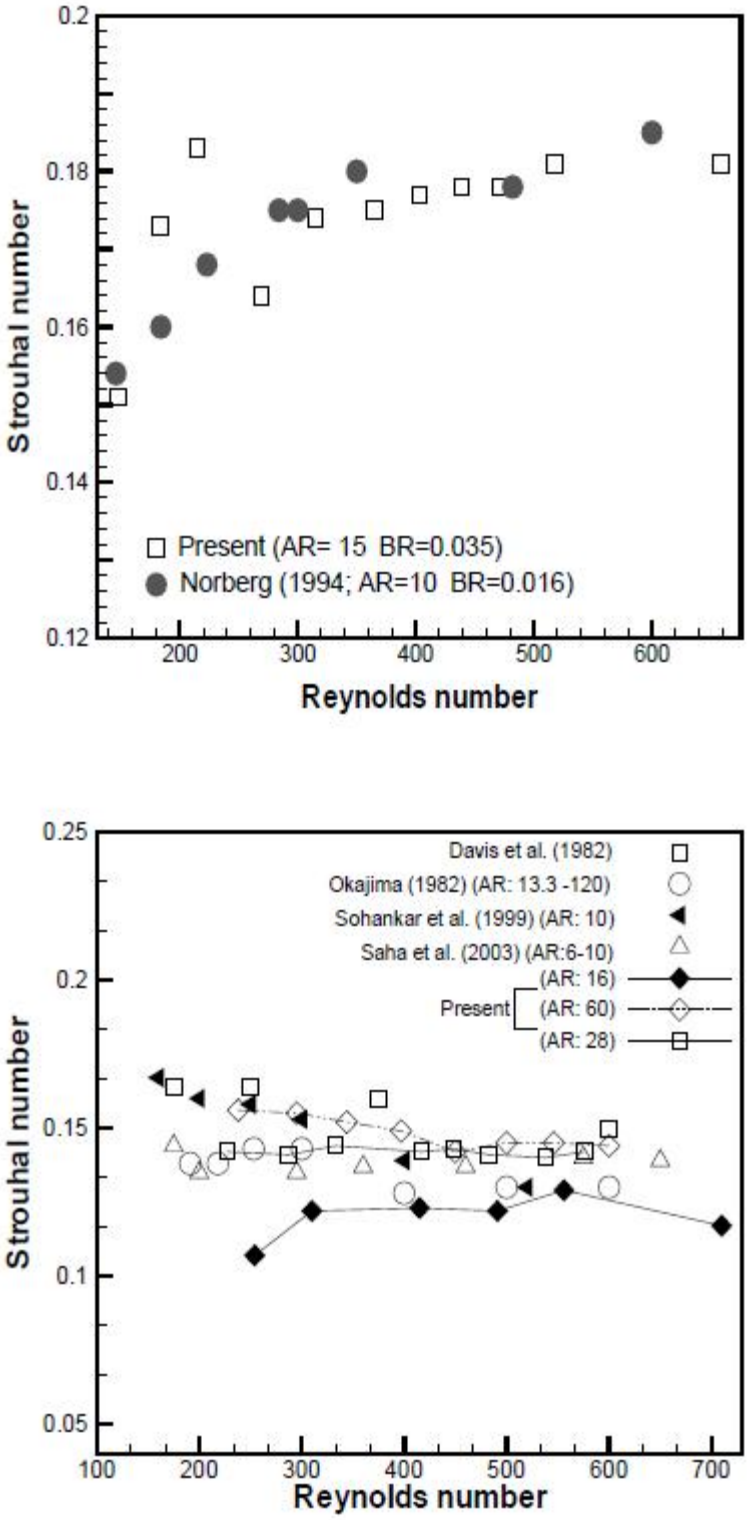

Figure 3.45: Comparison of Strouhal number as a function of Reynolds number for flow past circular (top) and square (bottom) cylinder at zero angle of incidence.

Previous Next

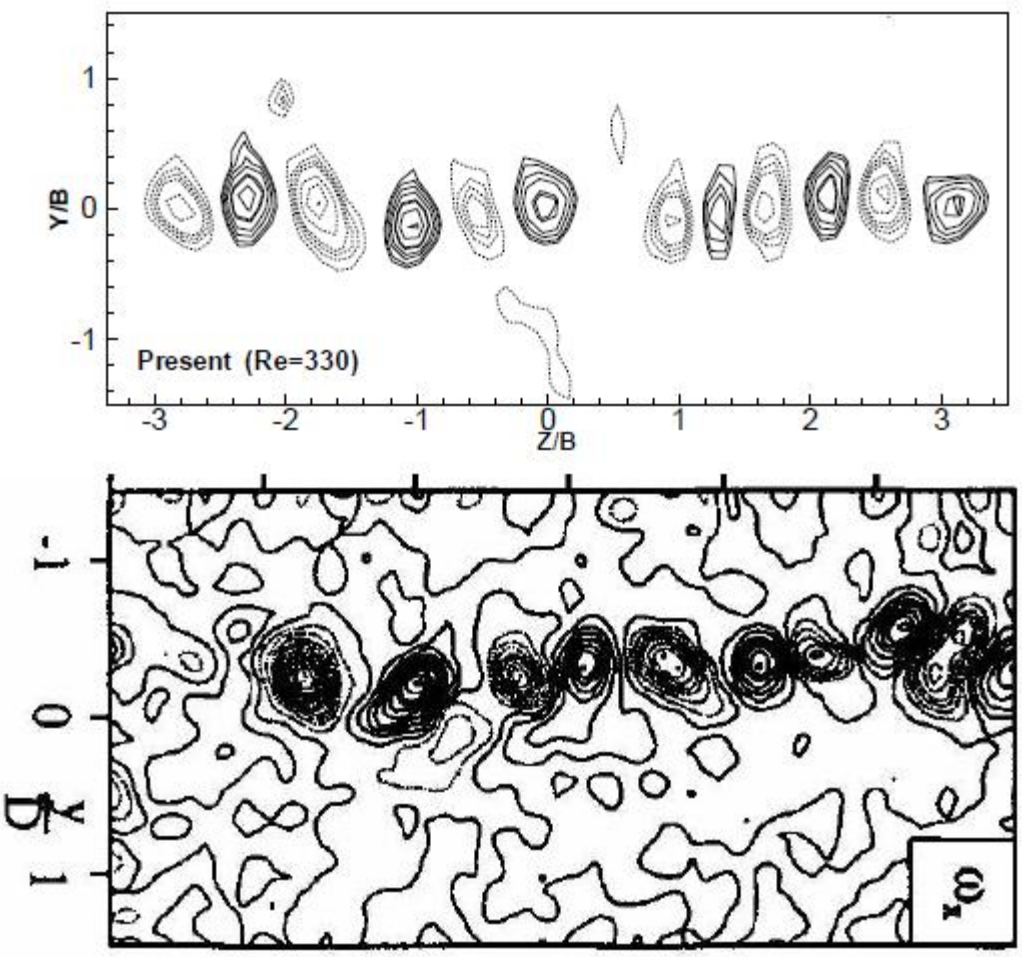

Figure 3.46: Comparison of instantaneous vorticity contours on the y-z plane above a circular cylinder. Top: present work, followed by the vorticity map of Brede et al. (1996)

Previous Next